Superconducting boron doped nanocrystalline diamond microwave coplanar resonator

Jerome A. Cuenca [a,*], Thomas Brien [a], Soumen Mandal [a], Scott Manifold [a], Simon Doyle [a], Adrian Porch [b], Georgina M. Klemencic [a], Oliver A. Williams [a,*]

[a] School of Physics and Astronomy, Cardiff University, Cardiff, Wales, CF24 3AA, UK
[b] School of Engineering, Cardiff University, Cardiff, Wales, CF24 3AA, UK

ARTICLE INFO

ABSTRACT

A coplanar waveguide resonator (CPR) is presented for kinetic inductance (L_k) and penetration depth (λ_L) measurements of superconducting boron doped nanocrystalline diamond (B-NCD) at microwave frequencies of 0.4 to 1.2 GHz and at temperatures below 3 K. Using finite element modelling and experimental measurements, this work demonstrates that thin granular B-NCD films (thickness $d \approx 500\,\text{nm}$) on Si have a large penetration depth ($\lambda_L \approx 3.8\,\mu\text{m}$), and therefore an associated high kinetic inductance per square ($L_{k,\square} \approx 670$ to $690\,\text{pH}/\square$). These values are much larger than those typically obtained for films on single crystal diamond, which is likely due to the high granularity of the nanocrystalline films. Based on the measured Q factors of the structure, the calculated surface resistance is found to be around ≈ 1 to $6\,\mu\Omega$ at $T < 2$ K in the 0.4 to 1.2 GHz range, demonstrating the potential for granular B-NCD for high quality factor superconducting microwave resonators and highly sensitive kinetic inductance detectors.

1. Introduction

Boron doped diamond (BDD) approaches metallic conductivity at concentrations in excess of 10^{20} cm^{-3} [1,2] and shows superconducting properties at low temperatures in excess of 10^{21} cm^{-3}, with an observed critical onset temperature (T_c) ranging between 3 to 5 K at zero field and a high type-II upper critical field ($H_{c,2}$) of up to 8 T [3–9]. BDD is typically grown using chemical vapour deposition (CVD) either on single crystal diamond substrates (B-SCD) or on Si to produce heavily granular nanocrystalline diamond films (B-NCD). These films can be made into superconducting quantum interference devices (SQUIDs) as demonstrated by Kageura et al. on B-SCD [8] and Bose et al. and Mandal et al. on B-NCD [7,10–12]. In order to understand the effective areas of BDD SQUIDs and also utilise BDD for other superconducting applications, such as microwave devices, further understanding of the magnetic penetration depth (λ_L), is needed. For B-SCD, moderate penetration depths have been observed ($\lambda_L \approx 0.2$ to $1\,\mu\text{m}$) [4,13]. However, for granular B-NCD, a recent study by Oripov et al. has demonstrated very large penetration depths ($\lambda_L \approx 2$ to $4\,\mu\text{m}$) in the microwave frequency range, thereby suggesting the possibility of highly sensitive microwave kinetic inductance (L_k) detectors [14]. The origin for the large penetration depths in B-NCD is most likely related to the granularity of the superconductor which is also observed for other materials; for example, non-granular aluminium films exhibit very

small penetration depths ($\lambda_L \approx 10$ to $30\,\text{nm}$ [15]), however granular aluminium films have much larger values ($\lambda_L \approx 0.3$ to $1.2\,\mu\text{m}$ [16]).

A method for investigating the penetration depth and kinetic inductance of materials is by using the coplanar waveguide resonator (CPR) method [17–20]. This approach involves patterning the superconductor into a planar microwave structure with a known resonant frequency and attributing differences to the designed frequency to the kinetic inductance, and therefore the penetration depth. Since superconducting films have a low surface resistance (R_s) at temperatures below T_c, high quality factor resonators can be obtained thereby offering a highly sensitive material measurement. Additionally, the CPR method is very convenient for CVD films since a CPR only requires one side of a substrate to be patterned without the need for any additional ground planes on the underside. The CPR method is less-widely reported for superconducting BDD, despite being a well-known approach for understanding L_k in a wide variety of materials including aluminium [21–23], niobium nitride [17] and yttrium barium copper oxide [18,19,24].

In this work the seemingly high L_k and λ_L of granular B-NCD is investigated using the microwave CPR method. Section 2 details from first principles the theoretical models for the estimation of L_k and R_s through the CPR resonant frequency and quality factor, respectively. A CPR design is presented with a known theoretical resonant frequency

---

based on the electrical length. Section 3 describes two finite element models (FEM) of the CPR; a 2D model for estimating the current distributions and a 3D model to identify the resonant modes and S-parameters of the structure. Section 4 details the device fabrication and characterisation process. Finally, Sections 5 and 6 detail the experimental results, including the film material characterisation using Raman spectroscopy and scanning electron microscopy (SEM) and the microwave device characterisation.

2. Theory

2.1. Kinetic inductance in coplanar structures

The phase velocity of signals along a transmission line can be defined as:

$$v_p = \frac{1}{\sqrt{\left(L_{\text{ext}} + L_{\text{int}}\right) C_{\text{ext}}}} \tag{1}$$

where L and C denote the inductance and capacitance per unit length, respectively, the subscript "ext" is associated with the external electric and magnetic fields in the space outside of the line's conductors, and the subscript "int" is associated with the internal fields. The internal inductance L_{int} can be expressed as the sum of two terms: $L_{\text{int}} = L_{\text{m}} + L_{\text{k}}$ where L_{m} is the magnetic inductance and L_{k} is the kinetic inductance. L_{m} is due to the finite magnetic field within the line's current-carrying conductors; however, it becomes small as the film thickness 'd' is reduced. L_{k} is associated with the non-dissipative kinetic energy of the "supercurrent" in superconducting films. L_{k} becomes the dominant contribution to L_{int} when d less than the magnetic penetration depth (λ_{L}) of the superconductor.

Superconductors with quasiparticle mean free paths smaller than λ_{L} are considered to be within the local London limit and electrodynamics are well-modelled by the London equations [25]. In this limit, L_{k} for a transmission line carrying a total current I over a cross-sectional area defined by S can be derived from first principles, starting with the kinetic energy stored per unit length [17]:

$$U_{\text{k}} = \frac{1}{2} L_{\text{k}} I^2 = \int_S \frac{1}{2} m_e |\bar{v}_s|^2 n_s dS \tag{2}$$

where m_e is the electron mass and $\bar{v}_s$ and n_s are the velocity and density, respectively, of the electron pairs making up the supercurrent (of current density $\bar{J}_s = n_s e \bar{v}_s$, where e is the fundamental charge of an electron). Rearranging for L_{k}, the general expression for the kinetic inductance per unit length is [26]:

$$L_{\text{k}} = \mu_0 \lambda_{\text{L}}^2 \left(\frac{\int_S |\bar{J}_s|^2 dS}{I^2} \right) \tag{3}$$

where μ_0 is the free space permeability and $\lambda_{\text{L}} = \sqrt{m_e / \mu_0 n_s e^2}$.

In the limit where λ_{L} is much larger than the thickness of the film, for an isolated rectangular superconducting strip the cross-sectional current density is almost uniform such that (3) can simply be approximated to [20]:

$$L_{\text{k}} \approx \frac{\mu_0 \lambda_{\text{L}}^2}{W d} \tag{4}$$

where W and d are the width and thickness of the rectangular strip, respectively. This simple formula for L_{k} can also be adapted for a coplanar waveguide (CPW) with symmetric ground planes where $d \ll \lambda_{\text{L}}$:

$$L_{\text{k}} \approx \frac{\mu_0 \lambda_{\text{L}}^2}{W d} \left(1 + \frac{W}{2 W_g} \right) \tag{5}$$

where W_g is the width of the ground planes. The correction term in brackets increases L_{k} by less than 10% for $W_g > 5$ W.

In the case where λ_{L} is much smaller than the film thickness, the current distribution on the line's cross-section becomes highly non-uniform, with current crowding along all of the film edges [20]. In this

instance, there is no simple analytical expression for L_{k} and thus the term in brackets in (3) needs to be computed numerically:

$$L_{\text{k}} \approx \frac{\mu_0 \lambda_{\text{L}}^2}{W d} g(W, S, d/\lambda) \tag{6}$$

where g is the geometrical function generated numerically by calculating the cross-sectional current distribution of the superconducting CPW, which depends on the gap 'S' between the centre conductor and ground plane.

The theory thus far considers the kinetic inductance contribution of a non-resonant CPW transmission line. To measure L_{k} with a high a degree of sensitivity, CPW transmission lines are typically fabricated into resonant structures by terminating a length of line l with open circuits at each end. This creates a half-wavelength CPR with resonant frequencies of integer multiples of the fundamental value:

$$f_0 = \frac{n}{2l} \frac{1}{\sqrt{L_{\text{ext}} C_{\text{ext}}}} \tag{7}$$

where n is the integer mode number. For a superconducting CPR where $L_{\text{k}} \gg L_{\text{m}}$, the fundamental resonant frequency decreases:

$$f_{\text{k}} \approx \frac{f_0}{\sqrt{1 + L_{\text{k}} / L_{\text{ext}}}} \tag{8}$$

For the purposes of estimating the S-parameters in FEM, the decrease in frequency caused by L_{k} can also be modelled as an effective contribution to the relative permeability:

$$f_{\text{k}} \approx \frac{n}{2l} \frac{1}{\sqrt{\mu_0 \varepsilon_0 \mu_{\text{r,eff}} \varepsilon_{\text{r,eff}}}} \tag{9}$$

where $\mu_{\text{r,eff}}$ is the modelled effective permeability taking into account the contribution from L_{k}, $\varepsilon_{\text{eff}} \approx \frac{1}{2} \left(\varepsilon_r + 1 \right)$ is the effective permittivity of the CPR [27] and ε_r is the relative permittivity of the substrate, ε_0 is the free space permittivity. All harmonics of the CPR are reduced by the same factor of $\sqrt{1 + L_{\text{k}} / L_{\text{ext}}}$ since the CPW is non-dispersive (i.e. λ_{L} is frequency independent and thus L_{k}, if the supercurrent conductivity is dominant over the quasiparticle conductivity, which is usually true for $T \ll T_c$). Thus, the reduction in frequency can be related to L_{k} of the film if the contribution from L_{ext} is known, which can be calculated analytically using conformal mapping with the well-known formulae [17,28]:

$$L_{\text{ext}} = \frac{\mu_0}{4} \mu_{\text{r,eff}} \frac{K\left(k'\right)}{K(k)} \tag{10}$$

$$C_{\text{ext}} = 4\varepsilon_0 \varepsilon_{\text{r,eff}} \frac{K(k)}{K(k')} \tag{11}$$

$$k = \frac{W}{W + 2S} \tag{12}$$

$$k' = \sqrt{1 - k^2} \tag{13}$$

where K is the complete elliptical integral of the first kind.

2.2. Surface resistance in coplanar structures

The surface resistance can be obtained using a similar derivation to L_{k}. First, consider the per unit length power dissipated in the transmission line:

$$P = \frac{1}{2} I^2 R = \Re \left(\frac{1}{\sigma_c} \right) \int_S |\bar{J}_s|^2 dS \tag{14}$$

where R is the per unit length resistance, $\sigma_c = \sigma_1 - j\sigma_2$ is the two-fluid model complex conductivity, σ_1 is associated with the quasiparticle or normal state conductivity and $\sigma_2 = 1/\mu_0 \omega \lambda_{\text{L}}^2$ is associated with the supercurrent or Cooper pair conductivity. In the limit where $\sigma_2 \gg \sigma_1$ which is typically found at $T \ll T_c$, (14) can be rearranged as:

$$R \approx \frac{\sigma_1}{\sigma_2^2} \left(\frac{\int_S |\bar{J}_s|^2 dS}{I^2} \right) \tag{15}$$

Note that the term within the brackets is the same as the term in (3) and therefore the ratio yields:

$$\frac{R}{L_k} \approx \frac{\sigma_1}{\sigma_2^2} \frac{1}{\mu_0 \lambda_L^2} \tag{16}$$

The surface resistance (R_s) is related to the above equation through σ_1 from the expression for the surface impedance in the two-fluid model:

$$R_s \approx \frac{1}{2} \sigma_1 \mu_0^2 \omega^2 \lambda_L^3 \tag{17}$$

Rearranging (16) for σ_1 and substituting into (17), an expression is obtained for R_s of the CPW transmission line:

$$R_s \approx \frac{1}{2} \mu_0 \lambda_L \frac{R}{L_k} \tag{18}$$

By fabricating a CPW into a resonant CPR structure, the unloaded quality factor (Q_0) can then be defined using the total per unit length inductance and resistance $Q_0 = \omega L / R$, thus the surface resistance can be obtained using the following [18]:

$$R_s \approx \mu_0 \lambda_L \frac{L}{L_k} \frac{1}{2Q_0} \tag{19}$$

In practice, the total inductance L is first calculated from the measured f_k and the known C_{ext}, followed by the determination of L_k and λ_L. These values along with the measured Q_0 are then used in (19) to obtain R_s.

2.3. Design of coplanar resonator

The CPR device used in this study is shown in Fig. 1 with a meandering transmission line of approximate length $l \approx 68.6$ mm on a 10×10 mm^2 substrate. The geometric parameters are: $W = 50\,\mu$m, $S = 5.6\,\mu$m, $d = 0.5\,\mu$m. In this CPR design the direct transmission approach has been used whereby power transmission only occurs at resonance when the device becomes superconducting. This is because standing waves are only formed at resonance with field maxima at the extremities where the coupling antennas are located. Typically, designs incorporate multiple CPR's tapped off of a feed-line, however, for a sensitive readout, the coupling reactance needs to be sufficiently large in order to observe the resonance minimum [20]. The coupling structures further load the resonator which results in a measured f and Q factor containing contributions from both the coupling antennas and the intrinsic resonance [28]. In the direct transmission approach, however, assuming a high dynamic range can be measured through the instrumentation, extremely weak coupling can be achieved such that the measured properties are approximated to the intrinsic resonance [29]. For simple material investigations, the direct approach is favourable, as to minimise unknown variability caused by the coupling structures for different materials.

3. Modelling

Two finite element models were used in this work, a 2D cross-sectional current density model and a 3D macroscopic frequency domain model. The current density model is used to determine a general solution for g in (6) for this CPR design, allowing determination of λ_L for a given L_k in both the small and large penetration depth limits. The 3D FEM solution is used to determine the resonant modes of the CPR meander design and the S-Parameters of the structure to ensure minimal interference from other resonances.

3.1. Current density model

The 2D current density model was developed in MATLAB$^®$ and uses the superconducting transmission line strip approach presented by Sheen et al. [26] that was later adapted to CPR structures by Porch et al. for details see [19]. Fig. 2 shows the calculated L_k and L_{ext} for the resonator geometry as a function of penetration depth. For this

$W = 50\,\mu$m
$S = 5.6\,\mu$m
$g = 5\,\mu$m
$d = 0.5\,\mu$m

10 mm

CPWR
$l \approx 68.6$ mm

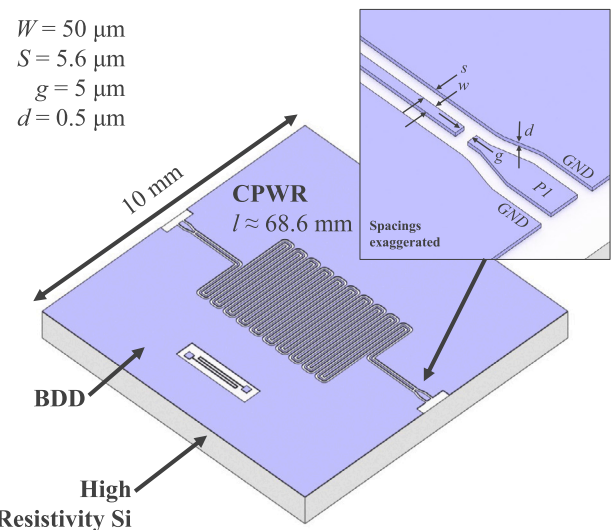Spacings exaggerated

BDD

High Resistivity Si

Fig. 1. 3D render schematic of the device layout (inset not to scale). 'P1' denotes port for the microwave signal lines and 'GND' denotes the ground planes.

geometry, L_k dominates the inductance at penetration depths of larger than ~2 μm. Additionally, Fig. 2(b) shows the current distribution at the top of the conductors for varying penetration depths, demonstrating that fairly uniform current distributions (i.e. where the normalised current density approaches unity on the centre conductor) are achieved at penetration depths of the order of several microns. In this limit, the simplified formula (5) can be applied. However, for penetration depths of a few hundred nanometres (the limit approaching $\lambda_L < d$) the current distribution significantly bunches towards the edges resulting in extremely high current densities. This current bunching is an unwanted effect as this results in very non-linear power dependent behaviour which complicates the extraction of L_k and R_s since the critical current density can be exceeded in these regions [20]. The lack of current crowding in the large penetration depth limit ($\lambda_L \gg d$) can be linked to linear behaviour when varying the power.

3.2. Macroscopic model

The 3D FEM solution was developed in COMSOL Multiphysics$^®$ using the eigenfrequency and frequency domain solvers. Briefly, a 2D work-plane was used to define the 10×10 mm^2 CPR lithography pattern. This work plane is sandwiched between two $10 \times 10 \times 0.5$ mm^3 domains, with the top defined as air ($\varepsilon_r = 1$) and the bottom as Si ($\varepsilon_r = 11.7$, $\tan \delta = 2 \times 10^{-4}$ [30]). The BDD layers are simulated as infinitely thin perfect electric conductors (PEC) with two multi-element lumped ports defined between the centre conductor pads and the ground planes. External boundaries are defined as PEC boundaries. The model is first run in the absence of any kinetic inductance (modelled as an effective permeability $\mu_{r,eff} = 1$) to obtain the unperturbed resonance. Subsequently, the kinetic inductance is introduced ($L_k = 0.1$ to $1.5\,\mu$H/m) by modelling all domains with an effective magnetic permeability defined by (8). An electromagnetic eigenfrequency study was used to estimate the resonant mode frequencies and a frequency domain study was used to estimate the typical wideband S-parameters of this structure. The FEM results are given in Fig. 3, showing the calculated eigenfrequencies in the gigahertz range for this geometry. The field distributions clearly show the first, second and third harmonics (868, 1736 and 2604 MHz). After introducing values as large as $L_k = 1.5\,\mu$H/m and $\lambda_L \approx 4.9\,\mu$m in the modelling, the fundamental resonant frequency decreases to a values as low as 336 MHz for this structure with similar fractional frequency shifts observed for the other modes.
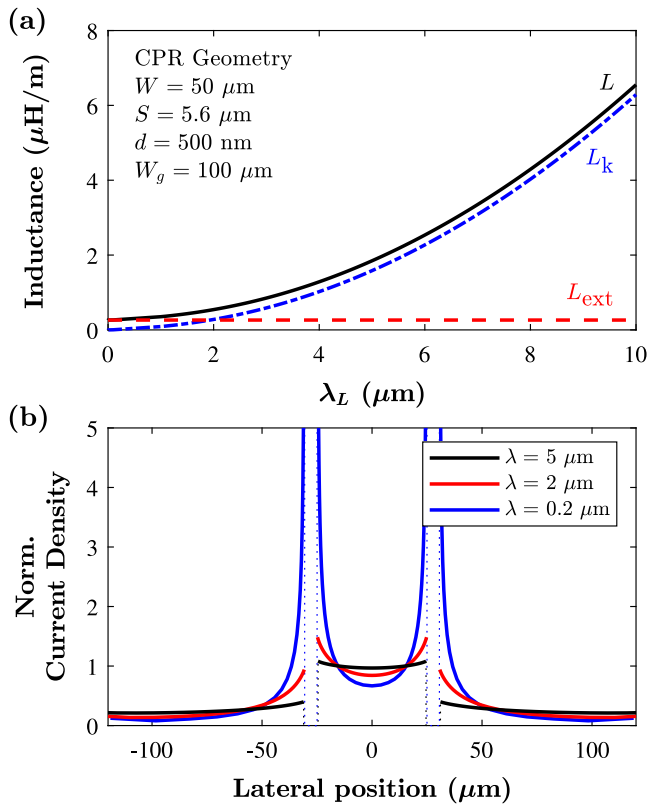
(a)

(b)

Fig. 2. Calculated inductance and surface current density of the proposed CPR design using the coupled transmission line model. (a) shows the total inductance contributions from the external and kinetic inductances with varying penetration depths and (b) shows the calculated current distribution at the top of the conductors for penetration depths of 5, 2 and $0.2\,\mu$m.

4. Method

B-NCD films were grown in a Seki Diamond Systems AX 6500 series microwave plasma CVD system. High resistivity float-zone Si substrates (⌀ = 2", $t = 500\,\mu$m) were first seeded using a nanodiamond colloid suspension [31–33] and grown at 3.5 kW at 40 Torr with a pyrometer measured substrate temperature of 755 °C for 3 h. Deposition was achieved in a gas mixture of CH_4, trimethylboron (TMB) dilute in H_2 in a total flow rate of 500 sccm (3% CH4 and B/C ratio ~12,800 ppm) [34].

The CPR device was patterned using a standard photolithography process (solvent cleaning and AZ nLof 2020 resist recipe with an adhesion promoter). A 100 nm nickel mask was evaporated onto the B-NCD using an Edwards 306 physical vapour deposition system with subsequent lift off. The samples were then etched in an O_2/SF_6 inductively coupled plasma (ICP) using an Oxford Instruments PlasmaPro 100 Cobra system. Scanning electron microscopy (SEM) images were obtained using a Hitachi SU8200 ($10\,kV$ at $10\,\mu$A) and Raman spectra was obtained using a Horiba LabRAM HR Evolution ($\lambda = 473, 532$ and $660\,nm$). Temperature dependent resistance measurements were also carried out on a separate piece of the same wafer using a Van der Pauw configuration in a Quantum Design physical property measurement system from 2 to 300 K .

The CPR device was cooled using custom-made cooling platform utilising a Cryomech PT-407-RM pre cooler and two Chase Research Cryogenics sorption fridges. The first sorption fridge, a helium-4–helium-3 pair, cools an intermediate stage to approximately 350 mK and acts the condensing point for the second sorption fridge, a single-shot helium-3 cooler, which cools the sample to ~300 mK with a hold time of approximately 36 h. The device readout was achieved via an RF chain which includes 20 dB and 10 dB attenuators on the input at the 50 K and 4 K stages of the cryostat, respectively, and a 10 MHz to 2 GHz low noise amplifier from Arizona State University. An additional amplifier was used for warm readouts (0.1–8.0 GHz, Narda-MITEQ AFS4-00100800-14-10P-4) and a programmable, 2-channel variable attenuator (Weinschel Aeroflex 8310); connected via an RF relay to a Rhode & Schwarz ZNB 20 VNA (used for S21 data and resonator parameter fitting).

5. Results

5.1. Material characterisation

Microscope and SEM images of the CPR device after ICP etching are shown in Fig. 4, showing the uninterrupted length of the transmission line structure with the capacitive coupling gaps at the edges of the sample. The SEM images show that in the gap regions, the B-NCD has been successfully etched which was also corroborated using a probe station measurement. Raman spectra is given in Fig. 5, showing the first and second order bands of Si at ~520 cm^{-1}and ~965 cm^{-1}, respectively [35–37] and numerous signatures typically associated with BDD at high dopant concentrations. The B-NCD bands are labelled at ~450 cm^{-1} (dA), ~1200 cm^{-1} (dC), ~1295 cm^{-1} (dB), 1332 cm^{-1} (d) and the wide region at ~1500–1680 cm^{-1} (G) is attributed to non-diamond carbon [38]. Fig. 5(a) shows that there is minimal variation in the spectra as a function of the laser excitation wavelength, where typically the G band is expected to become prominent at high laser wavelengths [35]. The magnified region given in Fig. 5 (b) shows a dotted line at 'd' where the characteristic zone centre phonon line at 1332 cm^{-1} of diamond should be, however, this peak has shifted significantly to ~1295 cm^{-1}, as denoted by 'dB'. This shift and asymmetry is a well-known signature of highly boron doped nano-crystalline films [34,38–41].

5.2. Device characterisation

The power transmission characteristics as a function of temperature are shown in Fig. 6. The broadband spectra shows that at 3 K mostly background noise floor is measurable. As T is lowered towards 300 mK, sharp resonances emerge at approximately 409, 813 and 1215 MHz, much lower than the designed frequencies of 868, 1736 and 2604 MHz, respectively. Using an effective kinetic inductance of $L_k \approx 0.93\,\mu$H/m, the FEM frequency domain $|S_{21}|^2$ traces demonstrate a plausible correlation with the experimental measurements. Additionally, the peak power transmission is low, demonstrating weak coupling. Magnified views of each resonance as a function of T are shown in Fig. 6(b) to (d) with each of the spectra fitted to a Lorentzian function to extract the measured resonant frequency and the loaded quality factor [42]:

$$|S_{21}|^2 = \frac{P_0}{1 + 4Q_L^2\left(\frac{f - f_m}{f_m}\right)^2} \tag{20}$$

where P_0 is the peak power at resonance, $Q_L = Q_U(1 - P_0)$ is the loaded quality factor and f and f_m are the frequency and the measured resonant frequency, respectively in Hz. Note that for all resonances, the peak transmitted power $P_0 \ll 0$ dB such that $Q_L \approx Q_U$ where the resonator is weakly coupled in this measurement apparatus, thus mitigating the need for any de-embedding of the coupling capacitance. The resonant frequency increases as T decreases and is observed to saturate as $T < 300$ mK with minimal back-bending. Nominal quality factors range from 4000 to 6000 at 300 mK, however, saturation was not observed owing to the limited T range. It is possible that the low temperature Q could actually be higher as $T \to 0$ K.

Power dependent measurements of each of the modes at 300 mK using variable attenuation from 40 to 20 dB are shown in Fig. 7. The resonant frequency and Q factor showed minimal change. Non-linear behaviour was not observed under these measurement conditions
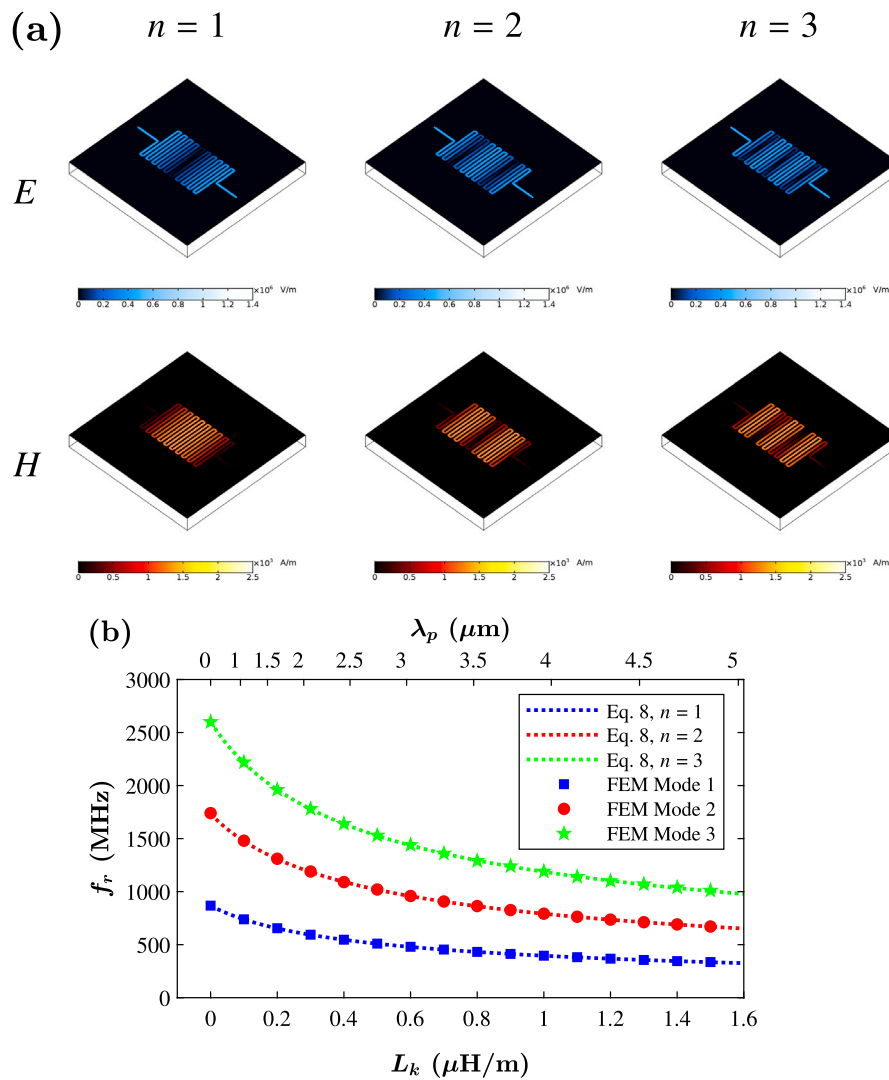
Fig. 3. 3D FEM eigenfrequency results (a) showing the electric field (top row) and magnetic field (bottom row) distribution for $n = 1, 2$ and 3 and the calculated resonant frequency as a function of L_k (bottom axes) and estimated λ_L (top axes) using the current density model.
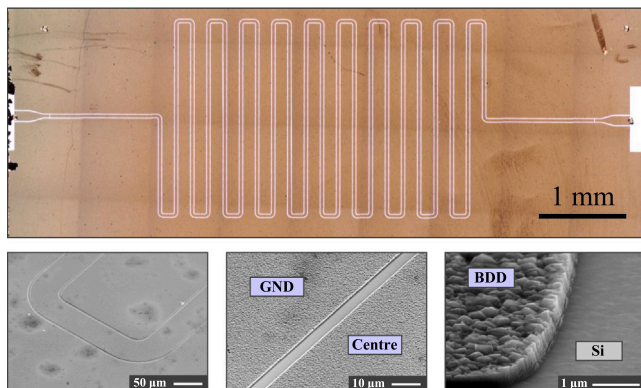

Fig. 4. Microscope and SEM images of the B-NCD CPR device.

implying a fairly uniform current distribution across the conductors and therefore, the simple model for L_k given in (5) is valid and giving further support of the case that the penetration depth is within the limit where $\lambda_L(T) \gg d$, or likely to be larger than ~500 nm [20].

Using (8), the estimated L_k and λ_L are shown in Fig. 8(a). Based on these frequency shifts, the extracted kinetic inductance is ~1.25 μH/m with an associated penetration depth of ~4.4 μm at 1.75 K and decreases to ~0.93 μH/m with an associated penetration depth ~3.8 μm at 300 mK. Since all harmonics are linked by n, similar values were obtained across other modes. To estimate the zero temperature penetration depth, temperature dependent models are required, with one of the most typical approaches being the empirical two fluid model as presented by Gorter and Casimir (GC):

$$\lambda_L(T) = \frac{\lambda_0}{\left[1 - \left(\frac{T}{T_c}\right)^\gamma\right]^{\frac{1}{2}}} \tag{21}$$

where λ_0 is the penetration depth at 0 K and $\gamma = 4$, though experimental measurements rarely exhibit this exponent depending on the type of superconductor [43]. T_c is estimated using the van der Pauw measurement in Fig. 8 (b), giving $T_c \approx 2.9$ K which is in agreement with B-NCD films grown in the same reactor at similar conditions ($T_c \approx 2.4$ to 4.5 K) [9,44,45]. Using this value and (21), the 0 K extrapolated values are given in Table 1 for $\gamma = 2.6$, as determined in the insert in Fig. 8(a). Similarly, the temperature dependent penetration depth can also be related to the superconducting gap energy through the BCS
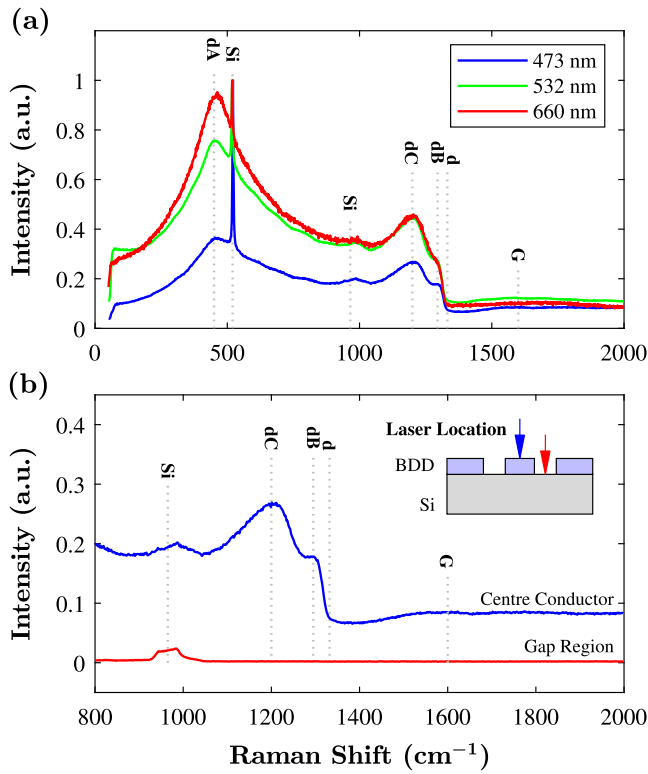
(a)

(b)

Fig. 5. Raman spectra of B-NCD CPR device: (a) Wide survey spectra of the centre conductor using 473, 532 and 660 nm excitation wavelengths and (b) shows a magnified region situated around the diamond 'd' band.

Table 1
Calculated zero temperature kinetic inductance per unit length and per square and penetration depth based on the CPR effective medium model.[a]

Mode, n	$L_{k,0}$ (μH/m) ± 0.006	$L_{k,\square}$ (pH/$\square$)[b] ± 5	λ_0 (μm) ± 0.02
1	0.921	671	3.79
2	0.934	681	3.82
3	0.943	687	3.84

[a]Error assumes a conservative measurement uncertainty in f_m of ± 1 MHz.
[b]Calculated by assuming $L_{k,\square} = L_{k,0} \times W/l$.

Table 2
Calculated zero temperature surface resistance and sheet resistance based on the CPR effective medium model.[a]

Mode, n	$R_{s,\text{eff}}$ ($\mu\Omega$) ± 0.01	$R_{s,\square}$ (nΩ/$\square$)[b] ± 0.01
1	1.3	0.95
2	3.2	2.33
3	5.7	4.15

[a]Error assumes a conservative measurement uncertainty in Q_U of ± 10.
[b]Calculated by $R_{s,\square} = R_{s,\text{eff}} \times W/l$.

low-temperature model [43]:

$$\lambda_L(T) = \lambda_0 \sqrt{\frac{\pi \Delta_0}{2k_B T}} \exp\left(\frac{-\Delta_0}{k_B T}\right) + \lambda_0 \tag{22}$$

where Δ_0 is the superconducting gap energy at 0 K and k_B is the Boltzmann constant. Fig. 8(a) shows the fit to $\lambda_L(T)$ using the same λ_0 as (21), yielding $\Delta_0 \approx 895\,\mu$eV. Finally, the surface resistance values obtained using (19) are given in Fig. 8(c) and Table Table 2, demonstrating that $R_s(T)$ decreases from 10 to 85 $\mu\Omega$ at 1.75 K to 1 to 6 $\mu\Omega$ at 300 mK (see Table 2).
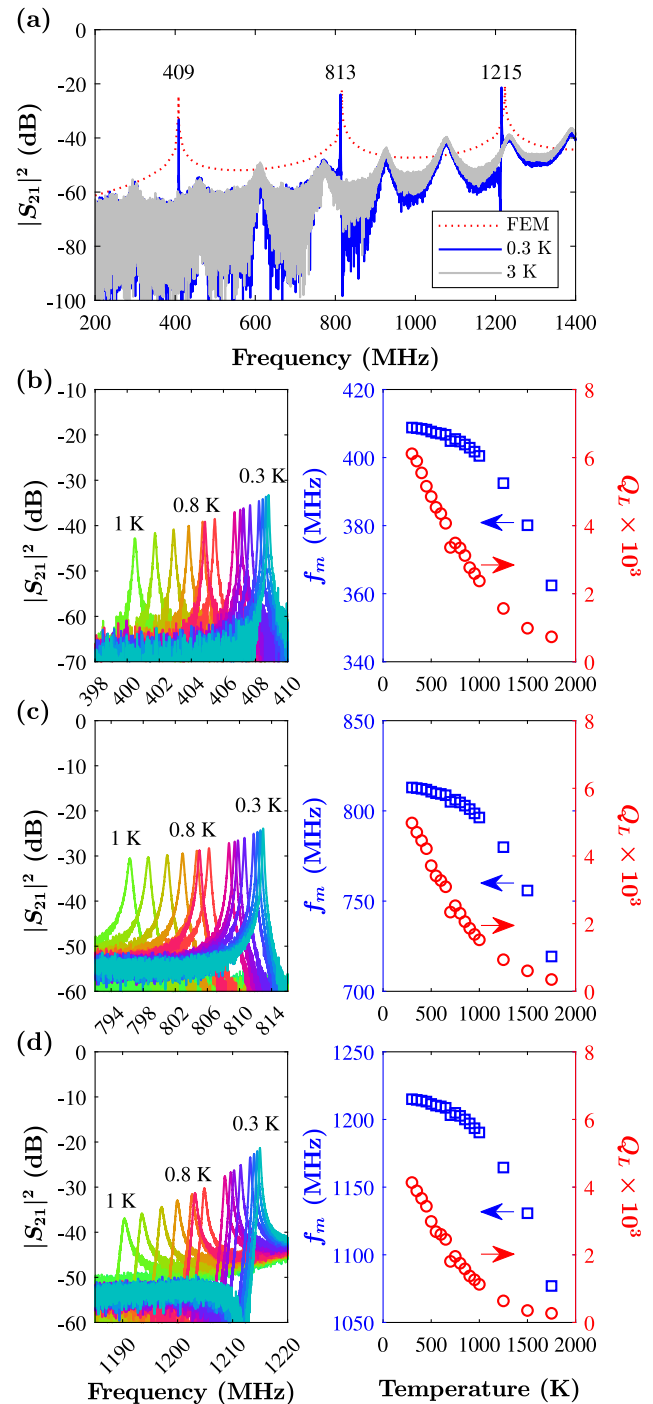
Fig. 6. Power transmission spectra of the B-NCD CPR at ($P_{\text{in}} = 0$ dBm with 20 dB variable attenuation and 30 dB RF line attenuation, for a total attenuation of 50 dB). (a) shows the wide $|S_{21}|^2$ spectra at 3 K (grey) and 0.3 K (blue) with an FEM result for $L_k \approx 0.93\,\mu$H/m (red dotted). (b) to (d) show magnified views of the 3 resonant modes from 1 K to 0.3 K and the fitted f_m and Q_L. (For interpretation of the references to colour in this figure legend, the reader is referred to the web version of this article.)

6. Discussion

The results presented here suggest that B-NCD films have large kinetic inductances and hence large penetration depths, far greater than the theoretical London penetration depths of BDD $\lambda_0 = (m_e/\mu_0 n e^2)^{1/2} \approx 168$ nm where m_e and e are the electron mass and charge, respectively and $n > 10^{21}$ cm^{-3}. The penetration depths are more consistent with
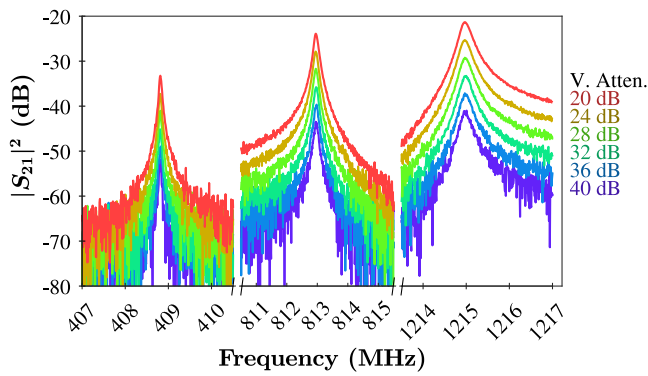
Fig. 7. Power transmission spectra of the B-NCD CPR at 300 mK at variable attenuation of each of the resonant modes. ($P_{in} = 0$ dBm with 40 to 20 dB variable attenuation; total line attenuation = 70 to 50 dB).
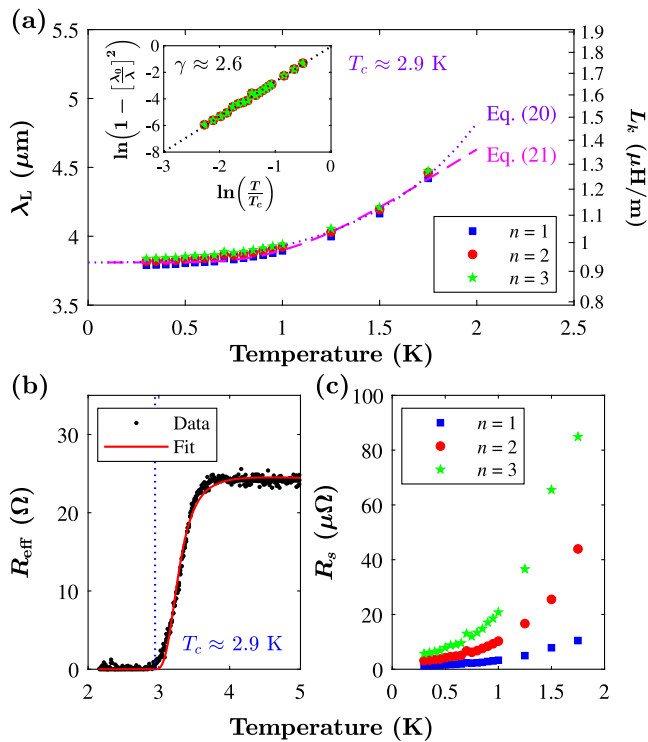

Fig. 8. Calculated superconducting properties of B-NCD CPR device. (a) shows the per unit length λ_L and L_k using (8), (b) shows the van der Pauw $R(T)$ curve for determination of T_c and (c) shows the calculated $R_s(T)$ from the CPR. Identification of T_c is denoted by the divergence in resistance (blue dotted). (For interpretation of the references to colour in this figure legend, the reader is referred to the web version of this article.)

those experimentally found in thin B-NCD films on Si substrates at a similar temperature ranges; $\lambda_L \approx 2$ to $4\,\mu m$ [14], however, less consistent with much thicker films or those measured on single crystal diamond substrates or B-SCD; $\lambda_L \approx 0.2$ to $1\,\mu m$ [4,13]. The results support the evidence that the granularity of the films plays a large role in increasing the penetration depth, and therefore its sensitivity for microwave kinetic inductance based devices. The laminar model presented by Hylton and Beasley considers the effect of large and small grain sizes on the effective penetration depth of granular superconductors. This model shows that polycrystalline materials in general have much larger effective penetration depths than single crystal materials. Klemencic et al. have previously demonstrated that B-NCD has characteristic signatures of a granular superconductor using the

Lerner, Varlamov and Vinokur model which exhibits clear dimensional transport signatures at temperatures above and approaching T_c [44]. Assuming that the grain boundaries in B-NCD can be considered as weak-links, the Hylton and Beasley laminar model is a reasonable explanation for the large measured penetration depths.

The temperature dependence of λ_L as described by (22) yields a γ exponent that tends towards that of an s-wave superconductor as is also demonstrated by Oripov et al. [14] and Sacépé et al. [46]. The extracted superconducting conducting gap of $\Delta_0 \approx 895\,\mu eV$ is large, however, is of similar magnitude to those reported by other measurement techniques. Ishizaka et al. obtained a gap of $\Delta_0 \approx 780\,\mu eV$ by laser excited photoemission spectroscopy, Sacépé et al. obtained $\Delta_0 \approx 285\,\mu eV$ by tunnelling spectroscopy and finally, Oripov et al. obtained a gap $\Delta_0 \approx 924\,\mu eV$ through microwave parallel plate resonator (PPR) [46,47].

The calculated surface resistance at $1\text{-}6\,\mu\Omega$ is not as low as measurements of YBCO at similar frequencies although at much lower temperatures since T_c for B-NCD is much lower [48]. Additionally, the calculated values here are much lower than those reported previously for B-NCD films in this frequency range, as is apparent by the higher observed quality factors [14]. Since the presented method and that of previous approaches using microwave PPR are both capable of measuring to similarly low values of R_s [18,49], the discrepancy may lie in the material deposition approach, i.e. by either microwave plasma assisted chemical vapour deposition (MP-CVD) vs hot filament chemical vapour deposition (HF-CVD). Grain boundaries are typically apparent in B-NCD films, irrespective of the deposition methodology, however, for films grown using MP-CVD, very low concentrations of non-diamond carbon are typically observed by the low G band in Raman spectroscopy, in contrast to those by HF-CVD [38,45,50]. This result suggests that while non-diamond carbon is well-known to introduce microwave losses at room temperature [51,52], incorporation into B-NCD films potentially creates significant microwave losses at low temperatures. Regardless, the measured quality factor of this device for B-NCD is still fairly low when compared to other material technologies based on aluminium [53,54] and niobium [55] at $Q_U > 10^4$. The cause of this is likely the substrate to which the B-NCD is deposited on; using the FEM model to reduce the loss tangent to zero yields Q factors $> 10^5$. High resistivity float-zone Si substrates are known to have additional losses at low T owing to potential hopping conduction [30]. Additionally, boron and carbon diffusion into the Si is likely to occur during the plasma assisted growth process resulting in an additional dielectric loss from the substrate [56–58]. Further improvements could potentially be made using substrates to stop diffusion, or more robust dielectrics that are less affected by microwave H_2 plasmas which are out of scope of this work.

7. Conclusion

This work demonstrates a measurement of the seemingly large penetration depth and low surface resistance of B-NCD using a microwave CPR approach with an effective medium model. Using a simple meander design with a weakly coupled power transmission technique, the intrinsic superconducting properties of thin B-NCD films can be obtained. This work demonstrates that B-NCD can be potentially used for superconducting microwave detection applications such as lumped kinetic inductance detectors (LEKIDs). This is because LEKIDs work on the principal where microwave photons break cooper pairs on the superconducting device which then results in a decrease in L_k and the frequency of microwave resonators. Since L_k is so high for B-NCD, this would potentially mean a larger frequency shift, and therefore a high sensitivity to microwave photons.

CRediT authorship contribution statement

Jerome A. Cuenca: Conceptualisation, Methodology, Software, Analysis, Investigation, Writing – original draft, Writing – review & editing, Data curation, Visualisation. **Thomas Brien:** Methodology, Investigation, Writing – review & editing. **Soumen Mandal:** Methodology, Resources, Writing – review & editing. **Scott Manifold:** Methodology, Writing – review & editing. **Simon Doyle:** Writing – review & editing, Supervision. **Adrian Porch:** Software, Analysis, Writing – review & editing, Supervision. **Georgina M. Klemencic:** Conceptualisation, Methodology, Analysis, Writing – review & editing, Supervision. **Oliver A. Williams:** Analysis, Funding acquisition, Writing – review & editing, Supervision.

Declaration of competing interest

The authors declare that they have no known competing financial interests or personal relationships that could have appeared to influence the work reported in this paper.

Data availability

Data associated with this work will be made available on the Cardiff University Research Portal

Acknowledgements

References

[1] W. Gajewski, P. Achatz, O.A. Williams, K. Haenen, E. Bustarret, M. Stutzmann, J.A. Garrido, Electronic and optical properties of boron-doped nanocrystalline diamond films, Phys. Rev. B Condens. Matter Mater. Phys. 79 (4) (2009) 1–14, http://dx.doi.org/10.1103/PhysRevB.79.045206.

[2] S.J. Cobb, Z.J. Ayres, J.V. Macpherson, Boron doped diamond: A designer electrode material for the twenty-first century, Annu. Rev. Anal. Chem. 11 (1) (2018) 463–484, http://dx.doi.org/10.1146/annurev-anchem-061417-010107.

[3] E.A. Ekimov, V.A. Sidorov, E.D. Bauer, N.N. Mel'nik, N.J. Curro, J.D. Thompson, S.M. Stishov, Superconductivity in diamond, Nature 428 (6982) (2004) 542–545, http://dx.doi.org/10.1038/nature02449.

[4] K. Winzer, D. Bogdanov, C. Wild, Electronic properties of boron-doped diamond on the border between the normal and the superconducting state, Phys. C Supercond. Appl. 432 (1–2) (2005) 65–70, http://dx.doi.org/10.1016/j.physc.2005.07.011.

[5] Y. Takano, M. Nagao, I. Sakaguchi, M. Tachiki, T. Hatano, K. Kobayashi, H. Umezawa, H. Kawarada, Superconductivity in diamond thin films well above liquid helium temperature, Appl. Phys. Lett. 85 (14) (2004) 2851–2853, http://dx.doi.org/10.1063/1.1802389.

[6] E. Bustarret, J. Kacmarčik, C. Marcenat, E. Gheeraert, C. Cytermann, J. Marcus, T. Klein, Dependence of the superconducting transition temperature on the doping level in single-crystalline diamond films, Phys. Rev. Lett. 93 (23) (2004) 2–5, http://dx.doi.org/10.1103/PhysRevLett.93.237005.

[7] S. Mandal, T. Bautze, O.A. Williams, C. Naud, É. Bustarret, F. Omnès, P. Rodière, T. Meunier, C. Bäuerle, L. Saminadayar, The diamond superconducting quantum interference device, ACS Nano 5 (9) (2011) 7144–7148, http://dx.doi.org/10.1021/nn2018396.

[8] T. Kageura, M. Hideko, I. Tsuyuzaki, A. Morishita, A. Kawano, Y. Sasama, T. Yamaguchi, Y. Takano, M. Tachiki, S. Ooi, K. Hirata, S. Arisawa, H. Kawarada, Single-crystalline boron-doped diamond superconducting quantum interference devices with regrowth-induced step edge structure, Sci. Rep. 9 (1) (2019) 2–8, http://dx.doi.org/10.1038/s41598-019-51596-w.

[9] G.M. Klemencic, S. Mandal, J.M. Werrell, S.R. Giblin, O.A. Williams, Superconductivity in planarised nanocrystalline diamond films, Sci. Technol. Adv. Mater. 18 (1) (2017) 239–244, http://dx.doi.org/10.1080/14686996.2017.1286223.

[10] M. Bose, D.L. Creedon, A. Barlow, M. Stuiber, G.M. Klemencic, S. Mandal, O. Williams, G. van Riessen, C.I. Pakes, Low-noise diamond-based D.C. NanoSQUIDs, ACS Appl. Electron. Mater. (2022) http://dx.doi.org/10.1021/acsaelm.2c00048.

[11] S. Mandal, C. Naud, O.A. Williams, E. Bustarret, F. Omnès, P. Rodière, T. Meunier, L. Saminadayar, C. Bäuerle, Nanostructures made from superconducting boron-doped diamond, Nanotechnology 21 (19) (2010) http://dx.doi.org/10.1088/0957-4484/21/19/195303.

[12] S. Mandal, C. Naud, O.A. Williams, É. Bustarret, F. Omnès, P. Rodière, T. Meunier, L. Saminadayar, C. Bäuerle, Detailed study of superconductivity in nanostructured nanocrystalline boron doped diamond thin films, Phys. Status Solidi (A) 207 (9) (2010) 2017–2022, http://dx.doi.org/10.1002/pssa.201000008.

[13] M. Ortolani, S. Lupi, L. Baldassarre, U. Schade, P. Calvani, Y. Takano, M. Nagao, T. Takenouchi, H. Kawarada, Low-energy electrodynamics of superconducting diamond, Phys. Rev. Lett. 97 (9) (2006) 097002, http://dx.doi.org/10.1103/PhysRevLett.97.097002.

[14] B. Oripov, D. Kumar, C. Garcia, P. Hemmer, T. Venkatesan, M.S. Ramachandra Rao, S.M. Anlage, Large microwave inductance of granular boron-doped diamond superconducting films, Appl. Phys. Lett. 118 (24) (2021) 242601, http://dx.doi.org/10.1063/5.0051227, arXiv:2103.14738.

[15] W.L. McLean, Superconducting penetration depth measurements in aluminium at 175 Mc/s, Proc. Phys. Soc. 79 (3) (1962) 572–585, http://dx.doi.org/10.1088/0370-1328/79/3/314.

[16] R.W. Cohen, B. Abeles, Superconductivity in granular aluminum films, Phys. Rev. 168 (2) (1968) 444–450, http://dx.doi.org/10.1103/PhysRev.168.444.

[17] K. Watanabe, K. Yoshida, T. Aoki, Kinetic inductance of superconducting coplanar waveguides, Japan. J. Appl. Phys. 33 (10R) (1994) 570–572, http://dx.doi.org/10.1143/JJAP.33.5708.

[18] K. Yoshida, K. Watanabe, T. Kisu, K. Enpuku, Evaluation of magnetic penetration depth and surface resistance of superconducting thin films using coplanar waveguides, IEEE Trans. Appl. Supercond. 5 (2) (1995) 1979–1982, http://dx.doi.org/10.1109/77.402973.

[19] A. Porch, M. Lancaster, R. Humphreys, The coplanar resonator technique for determining the surface impedance of YBa2Cu3O7-delta thin films, IEEE Trans. Microw. Theory Tech. 43 (2) (1995) 306–314, http://dx.doi.org/10.1109/22.348089.

[20] A. Porch, P. Mauskopf, S. Doyle, C. Dunscombe, Calculation of the characteristics of coplanar resonators for kinetic inductance detectors, IEEE Trans. Appl. Supercond. 15 (2 PART I) (2005) 552–555, http://dx.doi.org/10.1109/TASC.2005.849916.

[21] S. Doyle, P. Mauskopf, J. Naylon, A. Porch, C. Dunscombe, Lumped element kinetic inductance detectors, J. Low Temp. Phys. 151 (1–2) (2008) 530–536, http://dx.doi.org/10.1007/s10909-007-9685-2.

[22] T. Noguchi, A. Dominjon, Y. Sekimoto, Analysis of characteristics of Al MKID resonators, IEEE Trans. Appl. Supercond. 28 (4) (2018) 1–6, http://dx.doi.org/10.1109/TASC.2018.2809615, arXiv:1709.10421.

[23] W. Zhang, K. Kalashnikov, W.-S. Lu, P. Kamenov, T. DiNapoli, M. Gershenson, Microresonators fabricated from high-kinetic-inductance aluminum films, Phys. Rev. A 11 (1) (2019) 011003, http://dx.doi.org/10.1103/PhysRevApplied.11.011003, arXiv:1807.00210.

[24] H. How, R. Seeds, C. Vittoria, Microwave charactercistics of YBCO coplanar waveguide resonator, IEEE Trans. Magn. 28 (5) (1992) 2217–2219, http://dx.doi.org/10.1109/20.179448.

[25] D.a. Cardwell, D.S. Ginley, Handbook of superconducting materials edited by, Physics I (2003) 2174, http://dx.doi.org/10.1201/9781420034202.

[26] D. Sheen, S. Ali, D. Oates, R. Withers, J. Kong, Current distribution, resistance, and inductance for superconducting strip transmission lines, IEEE Trans. Appl. Supercond. 1 (2) (1991) 108–115, http://dx.doi.org/10.1109/77.84617.

[27] L.F. Chen, C.K. Ong, C.P. Neo, V.V. Varadan, V.K. Varadan, Microwave Electronics, John Wiley & Sons, Ltd, Chichester, UK, 2004, p. 470, http://dx.doi.org/10.1002/0470020466.

[28] M. Göppl, A. Fragner, M. Baur, R. Bianchetti, S. Filipp, J.M. Fink, P.J. Leek, G. Puebla, L. Steffen, A. Wallraff, Coplanar waveguide resonators for circuit quantum electrodynamics, J. Appl. Phys. 104 (11) (2008) 113904, http://dx.doi.org/10.1063/1.3010859, arXiv:0807.4094v1.

[29] M. Javaheri Rahim, T. Lehleiter, D. Bothner, C. Krellner, D. Koelle, R. Kleiner, M. Dressel, M. Scheffler, Metallic coplanar resonators optimized for low-temperature measurements, J. Phys. D: Appl. Phys. 49 (39) (2016) 395501, http://dx.doi.org/10.1088/0022-3727/49/39/395501.

[30] J. Krupka, J. Breeze, N.M. Alford, A.E. Centeno, L. Jensen, T. Claussen, Measurements of permittivity and dielectric loss tangent of high resistivity float zone silicon at microwave frequencies, in: 16th International Conference on Microwaves, Radar and Wireless Communications, MIKON 2006, Vol. 54, (11) 2007, pp. 3995–4001, http://dx.doi.org/10.1109/MIKON.2006.4345377.

[31] O.A. Williams, O. Douhéret, M. Daenen, K. Haenen, E. Osawa, M. Takahashi, Enhanced diamond nucleation on monodispersed nanocrystalline diamond, Chem. Phys. Lett. 445 (4–6) (2007) 255–258, http://dx.doi.org/10.1016/j.cplett.2007.07.091.

[32] O. Williams, Nanocrystalline diamond, Diam. Relat. Mater. 20 (5–6) (2011) 621–640, http://dx.doi.org/10.1016/j.diamond.2011.02.015, arXiv:0704.0701.

[33] S. Mandal, Nucleation of diamond films on heterogeneous substrates: a review, RSC Adv. 11 (17) (2021) 10159–10182, http://dx.doi.org/10.1039/d1ra00397f.

[34] S. Mandal, H.A. Bland, J.A. Cuenca, M. Snowball, O.A. Williams, Superconducting boron doped nanocrystalline diamond on boron nitride ceramics, Nanoscale 11 (21) (2019) 10266–10272, http://dx.doi.org/10.1039/C9NR02729G.

[35] S. Prawer, R.J. Nemanich, Raman spectroscopy of diamond and doped diamond, Phil. Trans. R. Soc. A 362 (1824) (2004) 2537–2565, http://dx.doi.org/10.1098/rsta.2004.1451.

[36] V.S. Sedov, A.K. Martyanov, A.A. Khomich, S.S. Savin, V.V. Voronov, R.A. Khmelnitskiy, A.P. Bolshakov, V.G. Ralchenko, Co-deposition of diamond and β-SiC by microwave plasma CVD in H2-CH4-SiH4 gas mixtures, Diam. Relat. Mater. 98 (July) (2019) 107520, http://dx.doi.org/10.1016/j.diamond.2019.107520.

[37] J.A. Cuenca, S. Mandal, E.L.H. Thomas, O.A. Williams, Microwave plasma modelling in clamshell chemical vapour deposition diamond reactors, Diam. Relat. Mater. (2022) Accepted, arXiv:2111.10258.

[38] V. Mortet, Z. Vlčková Živcová, A. Taylor, O. Frank, P. Hubík, D. Trémouilles, F. Jomard, J. Barjon, L. Kavan, Insight into boron-doped diamond Raman spectra characteristic features, Carbon 115 (2017) 279–284, http://dx.doi.org/10.1016/j.carbon.2017.01.022.

[39] I.P. Zibrov, V.P. Filonenko, Heavily boron doped diamond powder: Synthesis and rietveld refinement, Crystals 8 (7) (2018) 1–7, http://dx.doi.org/10.3390/cryst8070297.

[40] H. Nagasaka, Y. Teranishi, Y. Kondo, T. Miyamoto, T. Shimizu, Growth rate and electrochemical properties of boron-doped diamond films prepared by hot-filament chemical vapor deposition methods, E-J. Surface Sci. Nanotechnol. 14 (March) (2016) 53–58, http://dx.doi.org/10.1380/ejssnt.2016.53.

[41] N. Dubrovinskaia, L. Dubrovinsky, N. Miyajima, F. Langenhorst, W.A. Crichton, H.F. Braun, High-pressure / high-temperature synthesis and characterization of boron-doped diamond, Z. Naturforsch. B 61 (12) (2006) 1561–1565, http://dx.doi.org/10.1515/znb-2006-1213.

[42] D. Pozar, Microwave Engineering, fourth ed., 2005, pp. 1–756.

[43] R. Prozorov, R.W. Giannetta, Magnetic penetration depth in unconventional superconductors, Supercond. Sci. Technol. 19 (8) (2006) http://dx.doi.org/10.1088/0953-2048/19/8/R01.

[44] G.M. Klemencic, J.M. Fellows, J.M. Werrell, S. Mandal, S.R. Giblin, R.A. Smith, O.A. Williams, Fluctuation spectroscopy as a probe of granular superconducting diamond films, Phys. Rev. Mater. 1 (4) (2017) 1–5, http://dx.doi.org/10.1103/PhysRevMaterials.1.044801, arXiv:1706.05845.

[45] S.A. Manifold, G. Klemencic, E.L.H. Thomas, S. Mandal, H. Bland, S.R. Giblin, O.A. Williams, Contact resistance of various metallisation schemes to superconducting boron doped diamond between 1.9 and 300 K, Carbon 179 (2021) 13–19, http://dx.doi.org/10.1016/j.carbon.2021.02.079.

[46] B. Sacépé, C. Chapelier, C. Marcenat, J. Kačmarčik, T. Klein, M. Bernard, E. Bustarret, Tunneling spectroscopy and vortex imaging in boron-doped diamond, Phys. Rev. Lett. 96 (9) (2006) 1–4, http://dx.doi.org/10.1103/PhysRevLett.96.097006, arXiv:0510541.

[47] K. Ishizaka, R. Eguchi, S. Tsuda, T. Yokoya, A. Chainani, T. Kiss, T. Shimojima, T. Togashi, S. Watanabe, C.-T. Chen, C.Q. Zhang, Y. Takano, M. Nagao, I. Sakaguchi, T. Takenouchi, H. Kawarada, S. Shin, Observation of a superconducting gap in boron-doped diamond by laser-excited photoemission spectroscopy, Phys. Rev. Lett. 98 (4) (2007) 047003, http://dx.doi.org/10.1103/PhysRevLett.98.047003.

[48] Y. Wang, H.T. Su, F. Huang, M.J. Lancaster, Measurement of YBCO thin film surface resistance using coplanar line resonator techniques from 20 MHz to 20 GHz, IEEE Trans. Appl. Supercond. 17 (2) (2007) 3632–3639, http://dx.doi.org/10.1109/TASC.2007.899369.

[49] R.C. Taber, A parallel plate resonator technique for microwave loss measurements on superconductors, Rev. Sci. Instrum. 61 (8) (1990) 2200–2206, http://dx.doi.org/10.1063/1.1141389.

[50] D. Kumar, M. Chandran, M.S. Ramachandra Rao, Effect of boron doping on first-order Raman scattering in superconducting boron doped diamond films, Appl. Phys. Lett. 110 (19) (2017) http://dx.doi.org/10.1063/1.4982591.

[51] J.A. Cuenca, E.L.H. Thomas, S. Mandal, O.A. Williams, A. Porch, Microwave determination of sp2 carbon fraction in nanodiamond powders, Carbon 81 (1) (2015) 174–178, http://dx.doi.org/10.1016/j.carbon.2014.09.046.

[52] J.A. Cuenca, K.J. Sankaran, P. Pobedinskas, K. Panda, I.-N. Lin, A. Porch, K. Haenen, O.A. Williams, Microwave cavity perturbation of nitrogen doped nanocrystalline diamond films, Carbon 145 (2019) 740–750, http://dx.doi.org/10.1016/j.carbon.2018.12.025.

[53] W. Zhang, K. Kalashnikov, W.S. Lu, P. Kamenov, T. Dinapoli, M.E. Gershenson, Microresonators fabricated from high-kinetic-inductance aluminum films, Phys. Rev. A 11 (1) (2019) http://dx.doi.org/10.1103/PhysRevApplied.11.011003, arXiv:1807.00210.

[54] D. Kalacheva, G. Fedorov, A. Kulakova, J. Zotova, E. Korostylev, I. Khrapach, A.V. Ustinov, O.V. Astafiev, Improving the quality factor of superconducting resonators by post-process surface treatment, AIP Conf. Proc. 2241 (June) (2020) http://dx.doi.org/10.1063/5.0011900.

[55] J.M. Hornibrook, E.E. Mitchell, C.J. Lewis, D.J. Reilly, Parasitic losses in Nb superconducting resonators, Physics Procedia 36 (2012) 187–192, http://dx.doi.org/10.1016/j.phpro.2012.06.069.

[56] L. Shao, J. Liu, Q.Y. Chen, W.K. Chu, Boron diffusion in silicon: the anomalies and control by point defect engineering, in: Materials Science and Engineering R: Reports, Vol. 42, (3–4) 2003, pp. 65–114, http://dx.doi.org/10.1016/j.mser.2003.08.002.

[57] S. Mirabella, D. De Salvador, E. Napolitani, E. Bruno, F. Priolo, Mechanisms of boron diffusion in silicon and germanium, J. Appl. Phys. 113 (3) (2013) http://dx.doi.org/10.1063/1.4763353.

[58] K. Shenai, Diffusion profiles of boron implanted into plasma-etched silicon surfaces, IEEE Trans. Electron Devices 39 (5) (1992) 1242–1245, http://dx.doi.org/10.1109/16.129114.